NANO · MICRO small
www.small-journal.com

Regulating Bifacial Surface Potential of Perovskite Film Enables Efficient Perovskite Solar Cells Universal for Different Charge Transport Layers

*Hao Huang, Yingying Yang, Benyu Liu, Zhineng Lan, Min Wang, Huilin Yan, Shujie Qu, Fu Yang, Qiang Zhang, Peng Cui, and Meicheng Li**

Planar perovskite solar cells (PSCs) show huge promise as an efficient photovoltaic technology, where the inefficient carrier transport at the hetero-interface largely limits their performance advancement. Herein, bifacial surface potential regulation is realized in a monolithic perovskite film through interface doping, leading to optimized dual-interfacial energy level alignment. In a n-i-p planar device, the up-shift of Fermi level on the perovskite bottom surface is first achieved through bottom-up diffusion of Li^+. Then, vitamin D2 is incorporated into the methoxy-Phenethylammonium iodide (MeO-PEAI) passivator, which can neutralize the up-shift of the Fermi level of perovskite top surface induced by MeO-PEAI passivation and further induce its down-shift. Both experimental measurements and theoretical simulation reveal that the bifacial surface potential regulation effectively promotes interfacial carrier transport and reduces carrier recombination, enhancing the adaptability of efficient PSCs to different charge transport materials. Impressively, the PSCs with 2,2′,7,7′-Tetrakis [N, N-di(4-methoxyphenyl) amino]-9,9′-spirobifluorene (Spiro-OMeTAD) and 2,4,6-Trimethyl-N, N-diphenylaniline (PTAA) achieve efficiencies of 26.05% (certificated 25.80%) and 24.65%, respectively. Besides, the device can maintain 99% of its highest efficiency after aging more than 2200 h in ambient air with a relative humidity of ≈20%, showing excellent stability.

1. Introduction

Metal halide perovskite materials possess distinct advantages of high absorption coefficient, adjustable bandgap, long carrier transport distance, etc., making them one of the best candidates for preparing high-efficiency solar cells.[1–4] In recent years, Metal halide perovskite solar cells (PSCs) have made tremendous advances in power conversion efficiency (PCE) with the certificated PCE as high as 26.7%,[5] due to the massive research around structure innovation,[6,7] film deposition regulation,[8–10] interface passivation[11–13] and so on. However, compared to the Shockley–Queisser theoretical limit, there is space for further improvement. Considering that the short-circuit current (J_{SC}) is approaching the theoretical limit, further improvement in efficiency may mainly rely on the increment of fill factor (FF) and open circuit voltage (V_{OC}), both values closely relate to the interfacial carrier transport and collection.[14–16]

To promote the interfacial carrier transport and reduce carrier non-radiative recombination, necessary strategies have been reported, such as energy level modulation,[17–19] interfacial defect passivation,[18,20] and so on. Among the strategies, regulating the perovskite surface potential, especially when it can be accompanied by defect passivation, shows a significant effect on improving the efficiency of PSCs. For example, Jiang et al., reported a reactive surface engineering approach by introducing3-(aminomethyl)pyridine (3-APy) on the perovskite top surface, which can realize effective n-type doping with a reduced work function in the surface region, leading to an efficient over 25%.[21] Recently, a symmetrical bis(2-chloroethyl)ammonium cation ($B(CE)A^+$) was introduced on the perovskite top surface, which induces a favorable energy band alignment and strengthened defect healing, resulting in an impressive efficiency of 25.60%.[22] As a multi-layer device, the dual interfaces of perovskite film possess a vital influence on carrier transport and collection. Compared to the perovskite top surface, the perovskite bottom surface is buried by perovskite film itself, which brings difficulties to bottom surface regulation. Although there are reports to modify the buried interface, these strategies mainly focus on surface regulation of the electron transport layer (ETL) and interface defects passivation.[23,24] For example, the 2,2′bipyridyl-4,4′-dicarboxylic acid (HBPDC) was utilized to serve as an interfacial layer between SnO_2 and perovskite layer in PSCs. This HBPDC is revealed can passivate the surface defects and modify the energy level structure of SnO_2, leading to an efficiency

H. Huang, Y. Yang, Z. Lan, M. Wang, H. Yan, S. Qu, F. Yang, Q. Zhang, P. Cui, M. Li
State Key Laboratory of Alternate Electrical Power System with Renewable Energy Sources
North China Electric Power University
Beijing 102206, China
E-mail: mcli@ncepu.edu.cn
B. Liu
Beijing Huairou Laboratory
Beijing 101400, China

The ORCID identification number(s) for the author(s) of this article can be found under https://doi.org/10.1002/smll.202412129

DOI: 10.1002/smll.202412129

improvement from 22.43% to 25.41%.[25] Other organic materials, such as 4-chloro-3-sulfamoylbenzoic acid,[12] 3-amino-4-pyrazolecarboxylic acid,[26] 3-sulphonato-propyl acrylate potassium salt,[27] etc., have also been reported to modify the buried interface for achieving improved photovoltaic performance. Recently, bis(2-aminoethyl) ether (BAE) was utilized to serve as an interfacial molecule at the buried interface, and the Li_2CO_3 which has been reported to modify the interface was further utilized to harmonize the strength of the bilateral bonds of BAE, leading to PSCs with an efficiency surpassing 26.5% (certified as 26.31%) and improved stability.[28,29] Hence, it is still a challenge to controllably regulate the surface potential of the perovskite bottom. In the PSCs, the photo-generated electrons and holes separate and then transport to the ETL and hole transport layer (HTL), respectively, at opposite directions. This feature makes the efficient carrier transport not only on the charge transport layers with suitable energy level structure but also on the surface potential of perovskite film on both sides. At present, the efficiency of PSCs is striving to approach its theoretical value, the synergistic optimization of dual hetero-interface in the whole device is necessary for efficiency advancement. Based on the above thinking, it should be a feasible approach to tailor the surface potential of perovskite film's top surface and bottom surface, promoting the carrier transport at the dual interface and thereby improving the efficiency of PSCs.

Herein, we realized bifacial surface potential regulation in a monolithic perovskite film through interface doping to optimize the dual-interfacial energy level alignment, which shows a universal effect of performance improvement on the PSCs with different charge transport layers. Detailly, we first doped the bottom surface of perovskite film using Li^+ through a bottom-up diffusion, which induced an up-shift of the Fermi level, leading to an n-type transition. Then, we doped the perovskite surface by incorporating vitamin D2 (VD2) into the surface passivator of methoxy-Phenethylammonium iodide (MeO-PEAI). Various measurements indicate that the VD2 can suppress the up-shift of the Fermi level of perovskite films induced by conventional surface passivation of MeO-PEAI. Both experimental measurements such as Mott–Schottky analysis and theoretical simulation demonstrated that the bifacial surface potential regulation through the above sequential interfacial doping can promote the interfacial carrier transport and reduce interfacial carrier recombination. As a consequence, when using 2,2′,7,7′-Tetrakis [N, N-di(4-methoxyphenyl) amino]-9,9′-spirobifluorene (Spiro-OMeTAD as the HTL, the planar PSCs with TiO_2 and SnO_2 as the ETLs achieved champion PCEs of 25.50% and 26.05%, respectively, and when using the 2,4,6-Trimethyl-N, N-diphenylaniline (PTAA) as the HTL, planar PSCs with TiO_2 and SnO_2 as the ETLs achieved champion PCEs of 24.32% and 24.65%, respectively.

2. Results and Discussion

2.1. The Design of Bifacial Surface Potential Regulation of Perovskite Film

To promote the separation and transport of photo-generated carriers, we try to synergistically regulate the surface potential of both the perovskite top surface and bottom surface. Based on the regular structure of PSCs, we attempt to perform n-doping and p-doping on the bottom surface and top surface of perovskite film, respectively, optimizing the dual-interfacial energy level alignment. Metal ions have been broadly reported to dope perovskite film. Considering the doping property and diffusion property, we select the Li atom as the n-type dopant on the perovskite bottom surface. As shown in **Figure 1**, for performing n-doping on the bottom surface, we introduce lithium carbonate (Li_2CO_3) on the surface of TiO_2, leveraging the Li^+ diffusion to dope the bottom surface of perovskite film. The feasibility of this bottom-up diffusion of Li^+ atom has been reported in the previous report.[28] After depositing perovskite film, for performing p-doping on the perovskite surface, we introduce VD2 (the chemical structure shown in Figure S1, Supporting Information), an organic material that has been reported can achieve p-doping in perovskite,[30] on the perovskite surface, compatible with the surface passivation using MeO-PEAI. Through the sequential n-doping and p-doping on the bottom surface and top surface of perovskite film, respectively, it may be feasible to achieve bifacial surface potential regulation in a monolithic perovskite, which is expected to promote the interfacial carrier transport, further enhancing the photovoltaic performance of PSCs.

2.2. The Potential Regulation of Perovskite Bottom Surface

We introduced Li_2CO_3 on the surface of TiO_2 and then attempted to perform n-doping on the bottom surface of perovskite film through bottom-up diffusion of Li^+. After introducing Li_2CO_3 which has been confirmed to show a negligible effect on perovskite crystallization (Figure S2, Supporting Information), X-ray photoemission spectroscopy (XPS) was carried out to analyze its existence and chemical bonding state. For the convenience of description, the TiO_2 with Li_2CO_3 on its surface is named TiO_2-Li_2CO_3. As shown in **Figures 2a** and S3 (Supporting Information), compared to the Li 1s spectrum of TiO_2, a peak appears clearly at ≈54.8 eV in the Li 1s spectrum of TiO_2-Li_2CO_3, indicating the successful introduction of Li^+ on the surface of TiO_2-Li_2CO_3. We further analyzed the O 1s peak in the XPS spectra (Figure S4, Supporting Information), compared to the O 1s spectrum of TiO_2, the O 1s spectrum of TiO_2-Li_2CO_3 generates a new peak located at ≈532 eV, which corresponds to the CO_3^{2-} of TiO_2-Li_2CO_3.[31] It is reported that CO_3^{2-} can passivate oxygen vacancy defects on the TiO_2 surface through binding with Ti atoms,[32] which can be validated by the slight shift of Ti 2P peak after introducing the Li_2CO_3 (Figure S5, Supporting Information).

Combining the previous report[32] and experimental results of photoluminescence (PL) mapping and time of flight secondary ion mass spectrometry (TOF-SIMS), we analyzed the chemical state of Li_2CO_3 at the interface of TiO_2-Li_2CO_3/perovskite with the schematic diagram shown in Figure S6 (Supporting Information). The CO_3^{2-} can passivate unsaturated Pb^{2+} through bonding with the Pb^{2+} on the bottom surface of perovskite, which can be validated by the slightly higher PL intensity of perovskite film after peeling off from the substrate (Figures S7 and S8, Supporting Information) and the reduced the trap-field limit voltage (V_{TFL}) of the electron-only device (Figure S9, Supporting Information). As for Li^+, it can diffuse into perovskite film in a bottom-up manner, which can be confirmed by the measurements of TOF-SIMS (Figure S10, Supporting Information). After

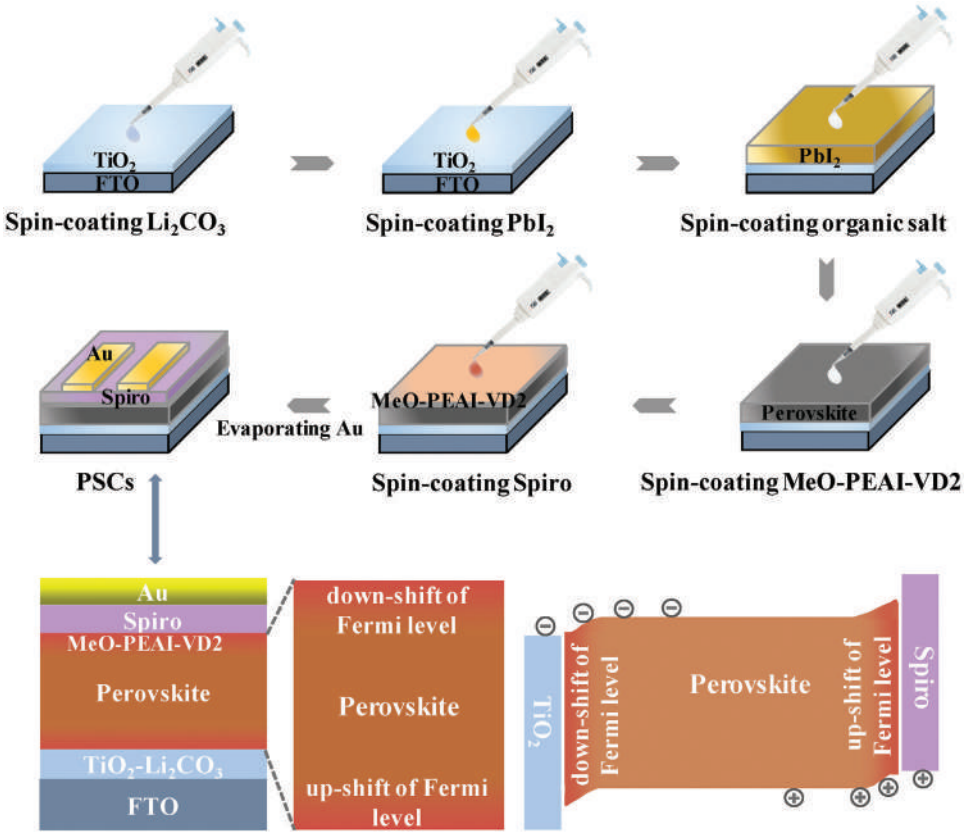

Figure 1. The schematic diagram of the fabrication process of PSCs, and the schematic diagram of bifacial surface potential regulation in a monolithic perovskite film.

confirming the diffusion of Li^+, we explored the doping effect of Li^+ on perovskite through density functional theory (DFT) calculations. After optimizing the structure model, the Li^+ mainly exists as an interstitial ion in the $FAPbI_3$ lattice (Figure 2b). The partial density of states (PDOS) of $FAPbI_3$ and Li-doped $FAPbI_3$ was also analyzed with the results shown in Figure 2c. It can be seen that after Li-doping, the Fermi level position of $FAPbI_3$ shows an up-shift, indicating a transition toward n-type. After peeling off the perovskite film from the substrate, we also measured the XPS valence band spectra of the bottom surface of perovskite on TiO_2 and TiO_2-Li_2CO_3, respectively. As shown in Figure 2d, after Li-doping, the Fermi level of the bottom surface of perovskite shows an obvious up-shift, confirming the n-type transition, which is consistent with the DFT results.

After confirming that the introduction of Li_2CO_3 at the TiO_2/$FAPbI_3$ interface can induce the n-type transition of perovskite bottom, we explored the interfacial electron transport using steady-state and time-resolved photoluminescence spectroscopy (PL and TRPL). After n-type doping on the perovskite bottom surface, the PL intensity of the corresponding perovskite film shows a significant quench, indicating the promoted interfacial electron transport (Figure 2e). Through fitting the TRPL spectra, the fast decay lifetimes of carriers in perovskite on TiO_2 and TiO_2-Li_2CO_3 are 75.01 and 47.92 ns, respectively (Figure 2f; Table S1, Supporting Information), further confirming that the n-type doping on the perovskite bottom can promote interfacial electron transport.

2.3. The Potential Regulation of Perovskite Top Surface

We now turn to discuss the potential regulation of perovskite top surface. Using PEAI and its derivatives to passivate the perovskite surface is a necessary step to fabricate high-efficiency PSCs since these passivation can largely improve the V_{OC}. However, the previous reports confirmed that the PEAI treatment may induce a negative work function shift (that is, more n-type), which causes the interfacial energetic mismatch and activates halide migration, resulting in inferior interfacial carrier transport and aggravated instability.[33,34] Based on the necessary surface passivation technology, we attempt to neutralize its negative effect on the perovskite surface potential. We incorporated VD2, an organic molecule that has been reported to serve as the p-type dopant in perovskite, into a passivator solution, where the passivator is MeO-PEAI in this work. Before investigating the effect of VD2 on surface potential, we confirmed that VD2 can slightly impede the formation of 2D perovskite (Figures S11 and S12, Supporting Information), however shows a negligible impact on the passivation effects using PL mapping measurements (Figure S13, Supporting Information). Then we performed Kelvin probe force microscopy (KPFM) on the perovskite surface. As shown in

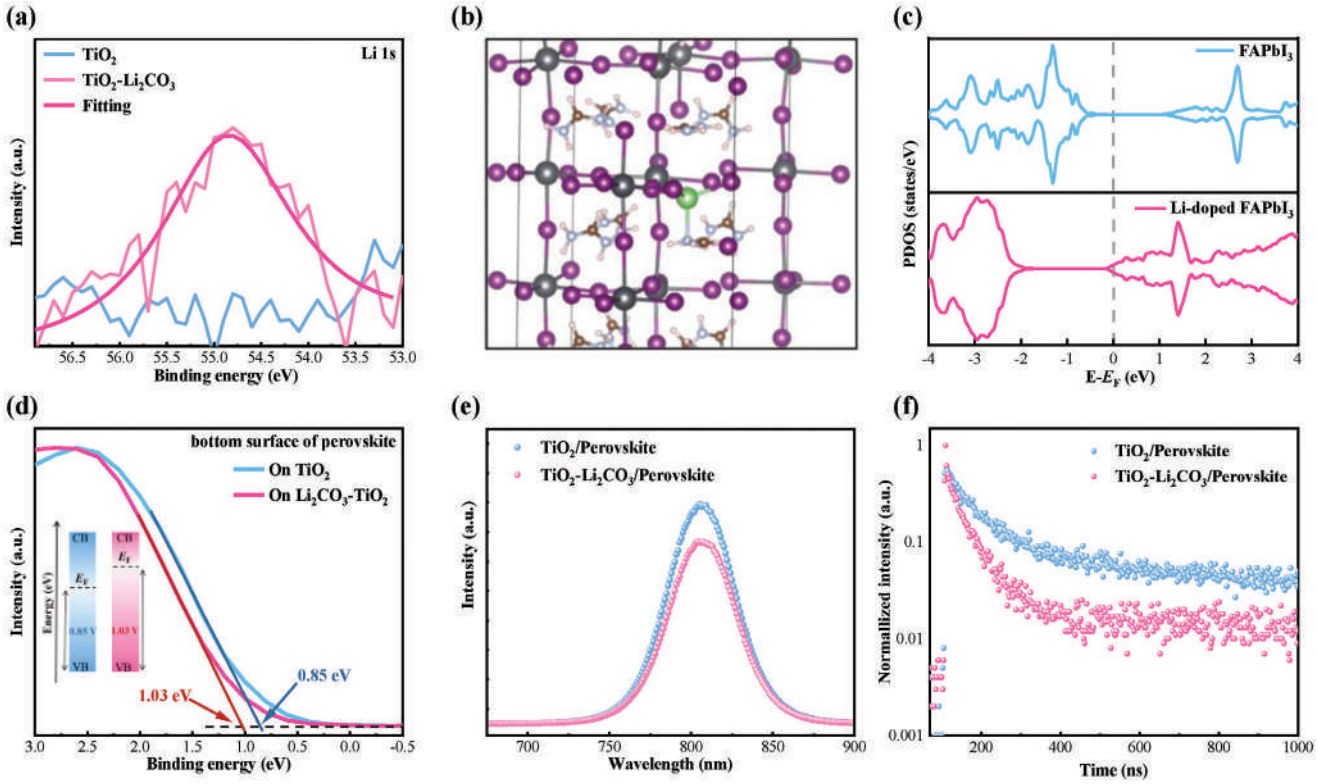

Figure 2. The potential regulation of perovskite bottom surface. a) Li 1s spectra of TiO_2 and TiO_2-Li_2CO_3. b) Optimized structure of Li-doped FAPbI3, the green ball is a Li atom. c) PDOS of $FAPbI_3$ and Li-doped $FAPbI_3$. d) XPS valence band spectra of the bottom surface of perovskite films. e) PL spectra of perovskite films. f) TRPL spectra of perovskite films.

Figure S14 (Supporting Information), the incorporated VD2 exhibits a slight influence on the surface morphology of perovskite film. Notably, the VD2 exhibits an obvious influence on the surface potential of perovskite film. We conducted a statistical analysis of the perovskite surface potential, in which the values of surface potential were extracted from Figure S14d–f (Supporting Information). As shown in **Figure 3a**, compared to perovskite, the surface potential of perovskite passivated by MeO-PEAI shows an obvious decrease from ≈0.70 to 0.62 V, indicating an up-shift of Fermi level (that is n-type transition), which is consistent with the previous reports.[35,36] After incorporating VD2 into MeO-PEAI, the induced up-shift of the Fermi level by MeO-PEAI is neutralized, and the Fermi level exhibits an additional down-shift (that is p-type transition). We also carried out measurements of XPS to characterize the valence band spectra of perovskite films. As shown in Figure 3b, the valence band spectra show that after MeO-PEAI passivation, the Fermi level of perovskite exhibits an up-shift, which is consistent with the results of KPFM. After passivating perovskite with MeO-PEAI-VD2, the Fermi level shows an obvious decrease compared to the Fermi level of perovskite, indicating that the VD2 not only can neutralize the up-shift of the Fermi level but also induces a down-shift of Fermi level, optimizing the interfacial energy level alignment.

We further investigated the influence of VD2 on interfacial hole transport at the perovskite/HTL interface, where the HTL is Spiro-OMeTAD. We fabricated the samples structured as FTO/perovskite/MeO-PEAI (or MeO-PEAI-VD2)/Spiro and then carried out measurements of PL and TRPL. As shown in Figure 3c and Table S2 (Supporting Information), after incorporating VD2, the fast decay lifetime of the carrier decreases from 177.11 to 87.12 ns, indicating the promoted interfacial hole transport. The PL mapping shown in Figure 3d was performed to validate the promoted interfacial hole transport, and more importantly shows the uniformity of interfacial carrier extraction. After incorporating VD2, the PL intensity not only shows an obvious quench but also exhibits a narrower distribution, which is consistent with the narrower distribution of surface potential shown in Figure 3a. The promoted interfacial carrier transport should be attributed to the optimized interface energy level alignment which resulted from the induced down-shift of Fermi level on the perovskite surface.

2.4. The Photovoltaic Performance of PSCs

We previously demonstrated that the bottom-up diffusion of Li^+ induces the up-shift of Fermi level on the perovskite bottom surface, and the utilization of VD2 induces the down-shift on the perovskite top surface, hence leading to a bifacial surface potential regulation in a monolithic perovskite film. In the following discussion, the untreated PSCs are labeled as the control sample, and the treated PSCs are labeled as the target sample. After determining the relatively optimal concentration of Li_2CO_3 and VD2 at the buried interface and top surface (Figure S15 and Tables S3

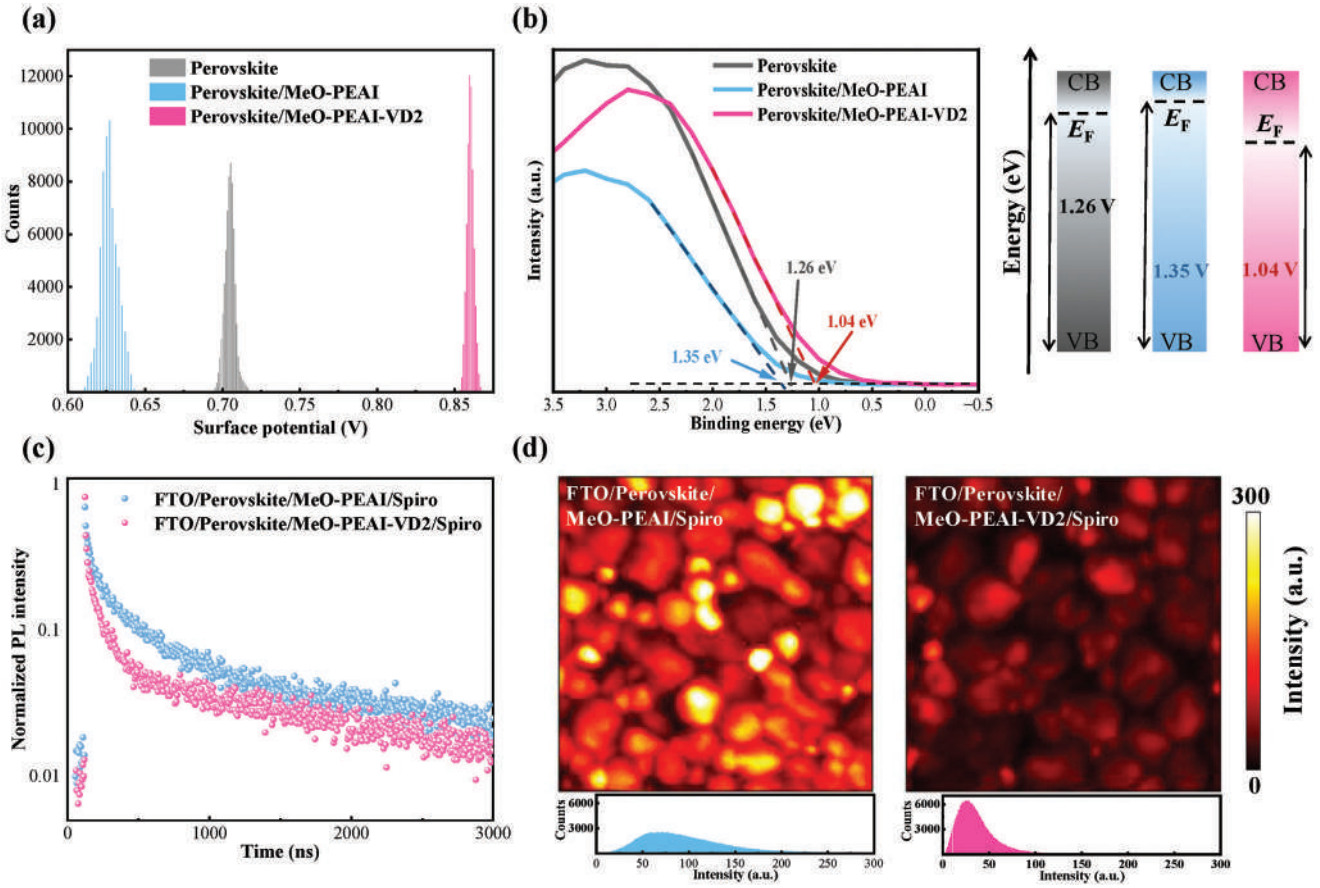

Figure 3. Characterization of potential regulation on perovskite surface. a) Histogram distribution of surface potential. b) XPS valence band spectra of perovskite surface (left) and corresponding schematic diagram of their energy level structure (right). c) TRPL spectra of perovskite films. d) PL mapping of perovskite films and the corresponding distribution of PL intensity.

and S4, Supporting Information), respectively, we fabricated the planar PSCs (F-doped tin oxide (FTO)/TiO_2/Perovskite/MeO-PEAI/Spiro-OMeTAD/Au) with bifacial surface potential regulation of perovskite film and then systematically characterized their physical property and photovoltaic performance. We fabricated a batch of control PSCs and target PSCs, respectively, and then collected their photovoltaic parameters, each batch includes 25 samples (**Figure** 4a; Figure S16, Supporting Information). Figure 4a shows the PCEs' distribution of control PSCs and target PSCs, where we can find out both types of PSCs possess good reproducibility and the target PSCs exhibit an obvious PCE improvement. Detailly, the average PCE of control PSCs is 23.92%. In comparison, the average PCE of target PSCs is 25.07%. Encouragingly, the target PSCs achieve a champion PCE of 25.50% (J_{SC} = 26.02 mA/cm^2, V_{OC} = 1.173 V, FF = 83.49%) with a negligible hysteresis (Figure 4b; Table S5, Supporting Information). In comparison, the control PSCs only achieve a champion PCE of 24.37%, with a J_{SC} of 25.99%, a V_{OC} of 1.161, and an FF of 80.78%. From the detailed photovoltaic parameters, we can find that the increment of PCE mainly results from the increased V_{OC} and FF, which should be due to the promoted interfacial carrier transport at the dual hetero-interfaces.

To gain an insight into the interfacial carrier transport and physical properties of PSCs, both experimental measurements and theoretical simulations were carried out. The results of the electrochemical impedance spectroscopy (EIS) confirm that the target PSCs possess a lower contact transport impedance and a higher recombination impedance, indicating the promoted interfacial carrier transport and reduced carrier recombination (Figure S17, Supporting Information), which is also validated by the results of the open-circuit photovoltage decay (OCVD) measurement (Figure S18, Supporting Information). The measurement of Mott–Schottky analysis which is utilized to probe the built-in field (V_{bi}) was also performed on control PSCs and target PSCs. As shown in Figure 4c, the V_{bi} of target PSCs is 0.96 V, which is higher than that (0.92 V) of control PSCs. This increased V_{bi} also explains the promoted interfacial carrier transport since the higher V_{bi} is beneficial for the separation and transport of photogenerated carriers. Besides, we calculated the ideal factor (n_{ID}) of both PSCs to explore the influence of bifacial surface potential regulation of perovskite film on PSCs performance according to the following equation:

$$V_{OC} = \frac{n_{ID} k_B T}{q} \ln(I) \quad (1)$$

where the k_B is the Boltzmann constant, T is the thermodynamic temperature, and q is the electron charge. The n_{ID} of

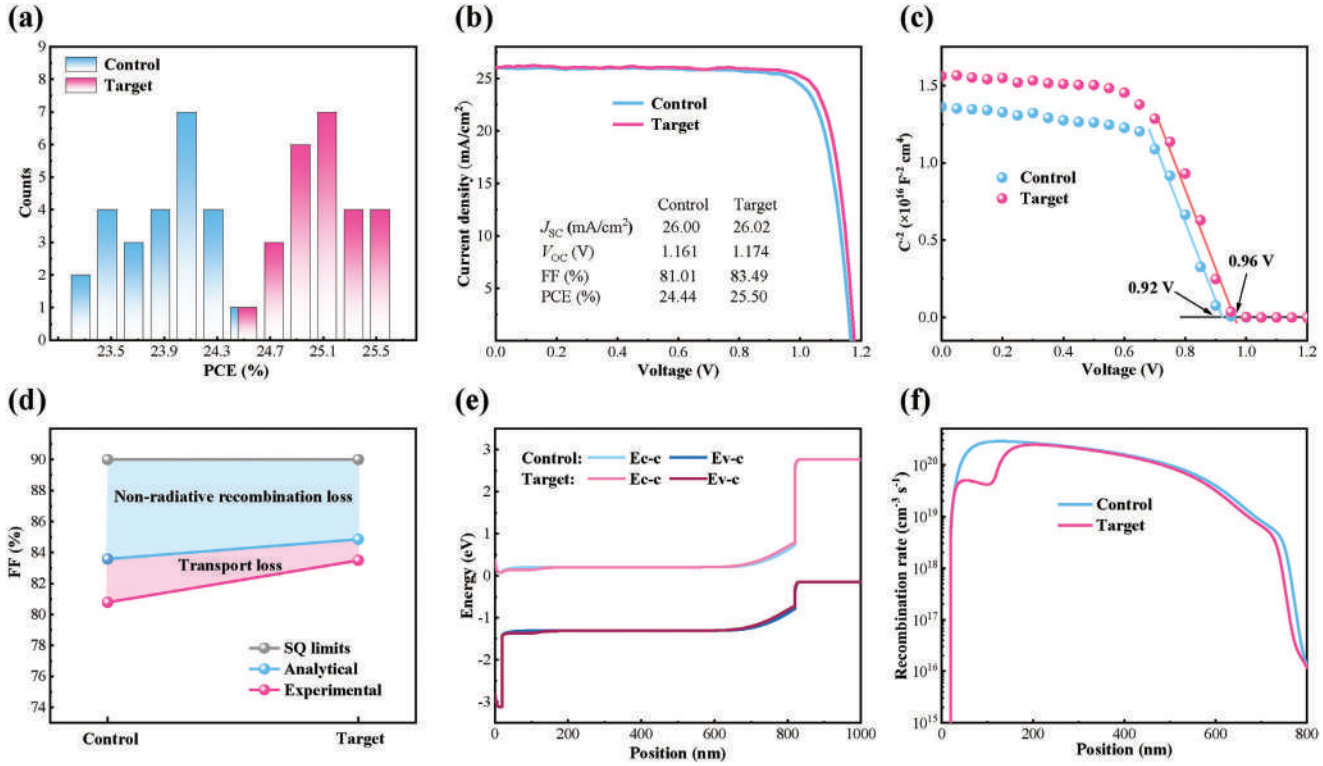

Figure 4. Photovoltaic performance of PSCs. a) Statistical results of PCEs (reverse scan) fitted from 25 control PSCs and target PSCs, respectively. b) *J–V* curves (reverse scan) of the champion control PSCs and target PSCs, the active area is 0.08 cm^2. c) Mott–Schottky plots of control PSCs and target PSCs. d) Plots of the SQ-limit FF, analytical FF, and the experimental FF for control PSCs and target PSCs. The FF limitation can be split into non-radiative recombination losses (blue area) and charge transport losses (pink area). e) The simulated energy band structure of control PSCs and target PSCs. f) The simulated recombination rate of control PSCs and target PSCs.

target PSCs is 1.65, which is lower than that (1.82) of control PSCs (Figure S19, Supporting Information), indicating the reduced non-radiative carrier recombination. Based on the calculated n_{ID}, we also calculated the analytical maximum FF to analyze the improvement of FF according to the following equation:[37]

$$FF_{max} = \frac{v_{oc} - \ln\left(v_{oc} + 0.72\right)}{v_{oc} + 1} \quad with \quad v_{oc} = \frac{qV_{OC}}{n_{ID}k_BT} \tag{2}$$

We then added the S-Q FF value and experimental FF value to make a direct comparison (Figure 4d). We can find that both the non-radiative recombination loss and transport loss decrease after regulating the bifacial surface potential of perovskite film, which may be attributed to the promoted interfacial carrier transport and reduced non-radiative carrier recombination. We also explore the influence of bifacial surface potential regulation on the device's physical property from a simulation perspective using the software of Solar Cell Capacitance Simulator-one Dimension with the simulation details shown in the Experimental Section and Table S6 (Supporting Information). Figure 4e shows the energy band structure calculated under one sun illumination. Compared to control PSCs, a downward band bending occurs at the perovskite bottom surface, and an upward band bending occurs at the perovskite top surface, which is conducive to the separation and oriented transport of photo-generated carriers. This promoted carrier separation and oriented transport further lead to reduced carrier recombination, especially at the perovskite bottom surface, which is validated by the calculation results of carrier recombination rates (Figure 4f).

2.5. Applications in Devices with Different Charge Transport Layers

The bifacial surface potential regulation of perovskite film induces a band bending of perovskite at dual hetero-interface, promoting the interfacial carrier transport, which may make it more compatible with different charge transport materials that possess different energy level structures. Hence, we first validate the improvement effects of our strategy on planar PSCs by fabricating and characterizing PSCs with SnO_2 as the ETL and 2,4,6-Trimethyl-N, N-diphenylaniline (PTAA) as the HTL, respectively. We collected photovoltaic parameters of a batch of (each batch includes 25 individuals) control PSCs and target PSCs, in which the ETL is SnO_2 and the HTL is Spiro-OMeTAD, and then made a statistical analysis. **Figure** 5a shows the distribution of PCEs and Figure S20 (Supporting Information) shows the distribution of J_{SC}, V_{OC}, and FF, respectively. The target PSCs possess excellent reproducibility with a higher average PCE of 25.57%. Impressively, the target PSCs achieve a champion PCE of 26.05%, which is higher than that (25.04%) of control PSCs, validating the positive effects of bifacial surface potential regulation on

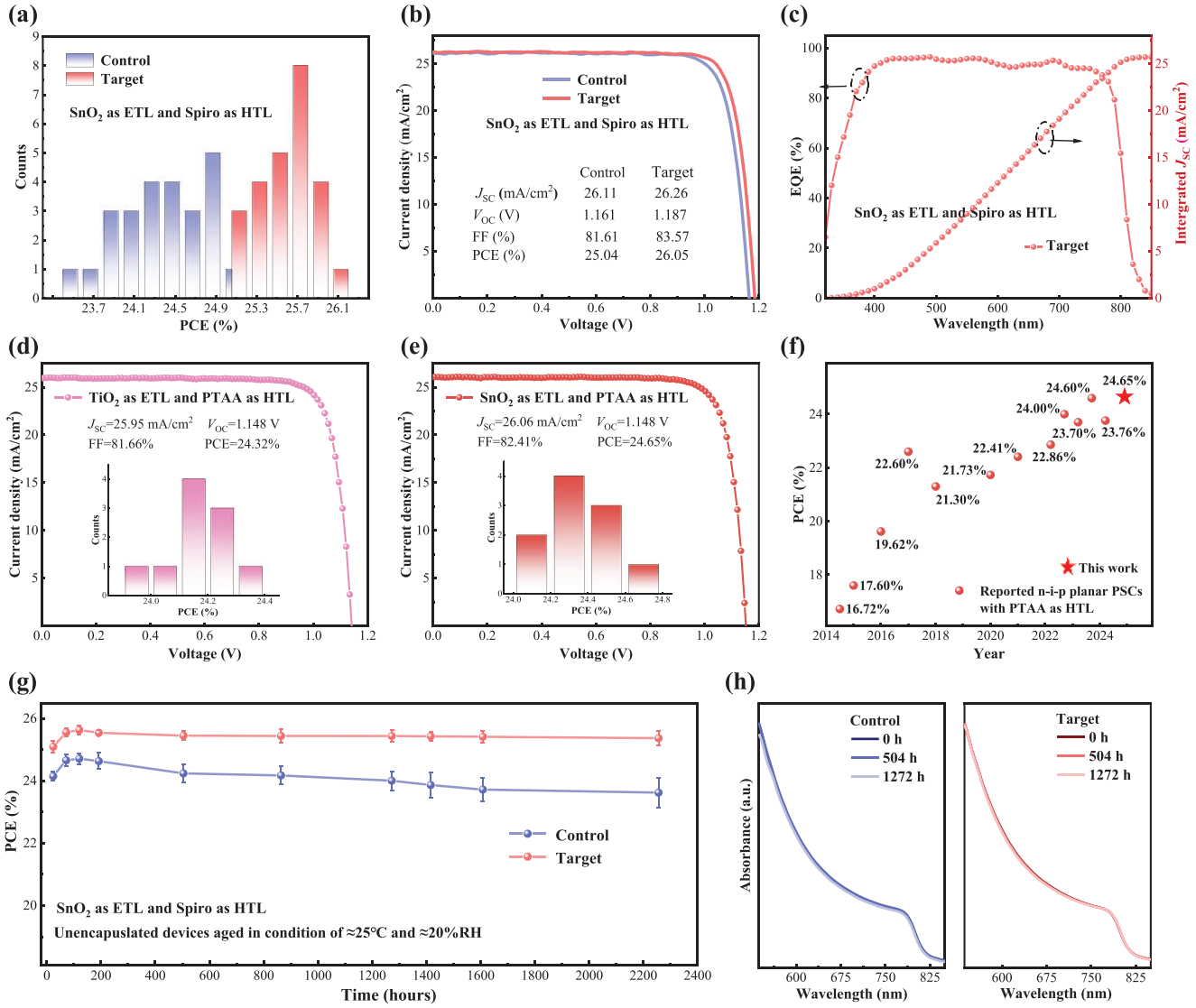

Figure 5. Performance of PSCs with different charge transport layers. a) Statistical results of PCEs (reverse scan) fitted from 25 control PSCs and target PSCs, respectively. b) *J–V* curves (reverse scan) of the champion control PSCs and target PSCs, the active area is 0.08 cm^2. c) EQE spectrum of target PSCs. d) *J–V* curves (reverse scan) of the target PSCs, in which the ETL is TiO_2 and the HTL is PTAA. The distribution of PCEs (10 individuals) is presented in the inset. e) *J–V* curves (reverse scan) of the target PSCs, in which the ETL is SnO_2 and the HTL is PTAA. The distribution of PCEs (10 individuals) is presented in the inset. f) Representative PCE of regular PSCs using PTAA as HTL reported in recent years. Detailed information is summarized in Table S5 (Supporting Information). g)The PCE evolution of unencapsulated devices. h) Operational stability of unencapsulated device under continuous 1-sun illumination in N_2 glovebox. Absorption spectra of perovskite films in control PSCs and target PSCs, these devices were stored in a condition of 25 °C and 20% RH.

improving PSCs efficiency (Figure 5b; Table S7, Supporting Information). The corresponding external quantum efficiency spectrum of target PSCs was also characterized and yielded integrated J_{SC} values with a small variation from the values obtained from *J–V* measurements (Figure 5c). Moreover, one of our best-performing PSCs has been validated by a third-party institute of the National Institute of Metrology, China (NIM, China), achieving a certified efficiency of 25.8% (Figure S21, Supporting Information). In short, the bifacial surface potential regulation on perovskite film is proven to be able to improve the PCE of planar PSCs by more than 26%, confirming its encouraging potential for fabricating ultra-high-efficiency PSCs.

This feasibility of bifacial surface potential regulation on fabricating high-efficiency PSCs was also demonstrated by the PSCs with PTAA as the HTL. Although the PTAA is reported to be more stable than Spiro-OMeTAD, the efficiency of planar n-i-p PSCs with PTAA as HTL is much lower than that of PSCs with Spiro-OMeTAD as HTL, in which the unsuitable energy level alignment with perovskite is one of the main reasons. In this work, when the ETL is TiO_2, the PTAA-based PSCs achieve a champion PCE of 24.32% with an average PCE of 24.17% (Figure 5d), and when the ETL is SnO_2, the PTAA-based PSCs achieve a champion PCE of 24.65% with an average PCE of 24.34% (Figure 5e). Notably, the obtained efficiency of 24.65% is the highest value of n-i-p

planar PSCs using PTAA as HTL reported to date, demonstrating the applicability of bifacial surface potential regulation on fabricating high-efficiency PSCs (Figure 5f; Table S8, Supporting Information).

To investigate the effect of bifacial surface potential regulation on device stability, both the PSCs and films were characterized during a continuous aging process. We first monitored the efficiency evolution of both devices that aged in ambient air at 25 °C and relative humidity (RH) of ≈20%. To relatively show a reproducible result, each group of samples used in this stability test includes 5 individuals. As shown in Figure 5g, both devices exhibit good stability upon exposure to ambient air for 2256 h. In detail, the target devices can maintain ≈99% of their highest efficiencies, the values obtained after sufficient oxidation of Spiro-OMeTAD. This phenomenon of PCE increment as the time prolongs at the early stage of aging is also shared by the control devices, and the control devices can maintain ≈96% of their highest values. Along with the device aging in ambient air, the stability of perovskite films stored in the same condition was also evaluated using the measurement of UV–vis spectroscopy (Figure 5h). Both films exhibit negligible decay of absorbance intensity, showing excellent storage stability, which is consistent with the results of device aging tests. Furthermore, the operational stability of unencapsulated under continuous one-sun illumination in the N_2 glovebox. As shown in Figure S22 (Supporting Information), the target device can maintain 84% of its initial efficiency after operating for 400 h, while the control device can maintain 76% of its initial efficiency, indicating slightly enhanced device stability. Based on the above discussion, compared to the slight effects on enhancing device stability, the bifacial surface potential regulation is more desirable for improving the efficiency of PSCs, especially considering its universal improvement on the photovoltaic performance of PSCs with different charge transport materials, supporting obtaining high-efficiency PSCs with PCE exceeding 26%.

3. Conclusion

In summary, bifacial surface potential regulation in a monolithic perovskite film was realized through interface doping, yielding a universal improvement in the photovoltaic performance of PSCs with different charge transport materials. Due to the promoted interfacial carrier transport and reduced interfacial carrier recombination demonstrated by the experimental measurements and theoretical simulation, the planar PSCs with TiO_2 as the ETL obtained a champion efficiency of 25.50%. Moreover, the planar PSCs with SnO_2 as the ETL obtained a champion efficiency of 26.05%, and the devices maintained ≈99% of their highest PCEs after storage in ambient air for 2256 h. It could be expected that our proposed bifacial surface potential regulation and the corresponding insight of the interfacial carrier dynamic provide an efficient approach and valuable guideline for breaking the bottleneck of efficiency improvement and achieving PSCs with ultra-high efficiency.

Supporting Information

Supporting Information is available from the Wiley Online Library or from the author.

Acknowledgements

H.H., Y.Y., and B.L. contributed equally to this work. This work is supported partially by the Key Research and Development Program sponsored by the Ministry of Science and Technology (MOST) (Grant nos. 2022YFB4200301), National Natural Science Foundation of China (Grant nos. 52232008, 52102245, 52072121, 52402254, and 22409061), Beijing Natural Science Foundation (2222076, 2222077), Beijing Nova Program (20220484016), Young Elite Scientists Sponsorship Program by CAST (2022QNRC001), 2022 Strategic Research Key Project of Science and Technology Commission of the Ministry of Education, Huaneng Group Headquarters Science and Technology Project (HNKJ20-H88), State Key Laboratory of Alternate Electrical Power System with Renewable Energy Sources (LAPS2024-05), the Fundamental Research Funds for the Central Universities (2022MS029, 2024MS036, 2022MS02, 2022MS031, 2023MS042, 2023MS047) and the NCEPU "Double First-Class" Program.

Conflict of Interest

The authors declare no conflict of interest.

Data Availability Statement

The data that support the findings of this study are available from the corresponding author upon reasonable request.

Keywords

high efficiency, interface energy level , interface doping, perovskite solar cells

Received: December 22, 2024
Revised: February 6, 2025
Published online:

[1] J. Huang, Y. Yuang, Y. Shao, Y. Yan, *Nat. Rev. Mater.* **2017**, *2*, 17042.
[2] F. Huang, M. Li, P. Siffalovic, G. Cao, J. Tian, *Energy Environ. Sci.* **2019**, *12*, 518.
[3] Z. Fan, K. Sun, J. Wang, *J. Mater. Chem. A* **2015**, *3*, 18809.
[4] S. D. Wolf, J. Holovsky, S. J. Moon, L. Philipp, B. Niesen, M. Ledinsky, F. J. Haug, J. H. Yum, C. Ballif, *J. Phys. Chem. Lett.* **2014**, *5*, 1035.
[5] National Renewable Energy Laboratory, "Best research-cell efficiency chart", www.nrel.gov/pv/cell-efficiency.html (accessed: December 2024).
[6] P. Cui, D. Wei, J. Ji, H. Huang, E. Jia, S. Dou, T. Wang, W. Wang, M. Li, *Nat. Energy* **2019**, *4*, 150.
[7] R. Azmi, D. S. Utomo, B. Vishal, S. Zhumagali, P. Dally, A. M. Risqi, A. Prasetio, E. Ugur, F. Cao, I. F. Imran, A. A. Said, A. R. Pininti, A. S. Subbiah, E. Aydin, C. Xiao, S. Seok, S. D. Wolf, *Nature* **2024**, *628*, 93.
[8] B. Jiao, Y. Ye, L. Tan, Y. Liu, N. Ren, M. Li, J. Zhou, H. Li, Y. Chen, X. Li, C. Yi, *Adv. Mater.* **2024**, *36*, 2313673.
[9] L. Yan, H. Huang, P. Cui, S. Du, Z. Lan, Y. Yang, S. Qu, X. Wang, Q. Zhang, B. Liu, X. Yue, X. Zhao, Y. Li, H. Li, J. Ji, M. Li, *Nat. Energy* **2023**, *8*, 1158.
[10] W. Zhao, D. Lin, P. Guo, N. Jia, J. Wu, Q. Ye, F. Yan, H. Wang, *Adv. Funct. Mater.* **2024**, 2423096.
[11] H. Chen, C. Liu, J. Xu, A. Maxwell, W. Zhou, Y. Yang, Q. Zhou, A. S. R. Bati, H. Wan, Z. Wang, L. Zeng, J. Wang, P. Serles, Y. Liu, S. Teale, Y. Liu, M. I. Saidaminov, M. Li, N. Rolston, S. Hoogland, T. Filleter, M. G. Kanatzidis, B. Chen, Z. Ning, E. H. Sargent, *Science* **2024**, *4*, 189.

[12] X. Wang, H. Huang, M. Wang, Z. Lan, P. Cui, S. Du, Y. Yang, L. Yan, Q. Zhang, S. Qu, M. Li, *Adv. Mater.* **2023**, *36*, 2310710.
[13] P. Guo, H. Zhu, W. Zhao, C. Liu, L. Zhu, Q. Ye, N. Jia, H. Wang, X. Zhang, W. Huang, V. A. Vinokurov, E. Ivanov, D. Shchukin, D. Harvey, J. M. Ulloa, A. Hierro, H. Wang, *Adv. Mater.* **2021**, *33*, 2101590.
[14] J. Peng, D. Walter, Y. Ren, M. Tebyetekerwa, Y. Wu, T. Duong, Q. Lin, J. Li, T. Lu, M. A. Mahmud, O. L. C. Lem, S. Zhao, W. Liu, Y. Liu, H. Shen, L. Li, F. Kremer, H. T. Nguyen, D. Y. Choi, K. J. Weber, K. R. Catchpole, T. P. White, *Science* **2021**, *371*, 390.
[15] J. J. Yoo, G. Seo, M. R. Chua, T. G. Park, Y. Lu, F. Rotermund, Y. K. Kim, C. S. Moon, N. J. Jeon, J. P. Correa-Baena, V. Bulović, S. S. Shin, M. G. Bawendi, J. Seo, *Nature* **2021**, *590*, 7847.
[16] H. Huang, P. Cui, Y. Chen, L. Yan, X. Yue, S. Qu, X. Wang, S. Du, B. Liu, Q. Zhang, Z. Lan, Y. Yang, J. Ji, X. Zhao, Y. Li, X. Wang, X. Ding, M. Li, *Joule* **2022**, *6*, 2186.
[17] W. Zhao, P. Guo, J. Wu, D. Lin, N. Jia, Z. Fang, C. Liu, Q. Ye, J. Zou, Y. Zhou, H. Wang, *Nano-Micro Lett.* **2024**, *16*, 191.
[18] X. Yue, X. Zhao, B. Fan, Y. Yang, L. Yan, S. Qu, H. Huang, Q. Zhang, H. Yan, P. Cui, J. Ji, J. Ma, M. Li, *Adv. Funct. Mater.* **2022**, *33*, 2209921.
[19] L. Ye, J. Wu, S. Catalán-Gómez, L. Yuan, R. Sun, R. Chen, Z. Liu, J. M. Ulloa, A. Hierro, P. Guo, Y. Zhou, H. Wang, *Nat. Commun.* **2024**, *15*, 78899.
[20] H. Wang, J. Wang, Q. He, J. Chang, S. Chen, C. Zhong, M. Wu, X. Zhao, H. Chen, Q. Tian, M. Li, J. Lai, Y. Yang, R. Li, B. Wu, W. Huang, T. Qin, F. Wang, *Angew. Chem., Int. Ed.* **2024**, *63*, 202404289.
[21] Q. Jiang, J. Tong, Y. Xian, R. A. Kerner, S. P. Dunfield, C. Xiao, R. A. Scheidt, D. Kuciauskas, X. Wang, M. P. Hautzinger, R. Tirawat, M. C. Beard, D. P. Fenning, J. J. Berry, B. W. Larson, Y. Yan, K. Zhu, *Nature* **2022**, *611*, 278.
[22] W. Shao, H. Wang, S. Fu, Y. Ge, H. Guan, C. Wang, C. Wang, T. Wang, W. Ke, G. Fang, *Adv. Mater.* **2024**, *36*, 2310080.
[23] Y. Yang, H. Huang, L. Yan, P. Cui, Z. Lan, C. Sun, S. Du, X. Wang, C. Yao, S. Qu, Q. Zhang, M. Wang, X. Zhao, M. Li, *Adv. Energy, Mater.* **2024**, *14*, 2400416.
[24] Y. Yang, R. Chen, J. Wu, Z. Dai, C. Luo, Z. Fang, S. Wan, L. Chao, Z. Liu, H. Wang, *Angew. Chem., Int. Ed.* **2024**, *63*, 202409689.
[25] M. Zhao, W. Gu, K. Jiang, X. Jiao, K. Gong, F. Li, X. Zhou, Y. Song, *Angew. Chem., Int. Ed.* **2024**, *137*, 202418176.
[26] Y. Chen, Q. Wang, W. Tang, W. Qiu, Y. Wu, Q. Peng, *Nano Energy* **2023**, *107*, 108154.
[27] C. Xu, S. Zhang, W. Fan, F. Cheng, H. Sun, Z. Kang, Y. Zhang, *Adv. Mater.* **2023**, *35*, 2207172.
[28] Q. Zhuang, H. Wang, C. Zhang, C. Gong, H. Li, J. Chen, Z. Zang, *Nano Res.* **2022**, *15*, 5114.
[29] Q. Li, H. Liu, C. Hou, H. Yan, S. Li, P. Chen, H. Xu, W. Yu, Y. Zhao, Y. Sui, Q. Zhong, Y. Ji, J. Shyue, S. Jia, B. Yang, P. Tang, Q. Gong, L. Zhao, R. Zhu, *Nat. Energy* **2024**, *9*, 1506.
[30] B. Liu, Y. Wang, Y. Wu, Y. Zhang, J. Lyu, Z. Liu, S. Bian, X. Bai, L. Xu, D. Zhou, B. Dong, H. Song, *Adv. Energy Mater.* **2022**, *13*, 2203352.
[31] Y. Zhang, T. Kong, H. Xie, J. Song, Y. Li, Y. Ai, Y. Han, D. Bi, *ACS Energy Lett.* **2022**, *7*, 929.
[32] M. Kim, I. Choi, S. J. Choi, J. W. Song, S. Mo, J. An, Y. Jo, S. Ahn, S. K. Ahn, G. Kim, D. S. Kim, *Joule* **2021**, *5*, 659.
[33] J. W. Lee, S. Tan, S. I. Seok, Y. Yang, N. Park, *Science* **2022**, *375*, eabj1186.
[34] S. Tan, T. Huang, I. Yavuz, R. Wang, T. W. Yoon, M. Xu, Q. Xing, K. Park, D. Lee, C. Chen, R. Zheng, T. Yoon, Y. Zhao, H. Wang, D. Meng, J. Xue, Y. J. Song, X. Pan, N. Park, J. Lee, Y. Yang, *Nature* **2022**, *605*, 268.
[35] U. Gunes, F. V. Yaylali, Z. G. Karabag, X. Gao, O. A. Syzgantseva, A. Karabag, G. B. Yildirim, K. Tsoi, N. Shibayama, H. Kanda, A. I. Rafieh, L. Zhong, A. Zuttel, P. J. Dyson, S. Yerci, M. K. Nazeeruddin, G. Gunbas, *Cell Rep. Phys. Sci.* **2023**, *4*, 101380.
[36] X. Wang, H. Huang, M. Wang, Z. Lan, Y. Yang, P. Cui, S. Du, L. Yan, Q. Zhang, S. Qu, Z. Zhao, M. Li, *Small* **2024**, *20*, 2312067.
[37] Q. Cao, Y. Li, H. Zhang, J. Yang, J. Han, T. Xu, S. Wang, Z. Wang, B. Gao, J. Zhao, X. Li, X. Ma, S. M. Zakeeruddin, W. E. I. Sha, X. Li, M. Grätzel, *Sci. Adv.* **2021**, *7*, eabg0633.